RF photonic downconversion of vector modulated signals based on a millimeter-wave coupled electrooptic nonlinear polymer phase-modulator

PARK, DONGHUN; PAGÁN, VINCENT R.; CHO, PAK S.; LUO, JINGDONG; JEN, ALEX K.-Y.; PETRUZZI, PAUL V.

Published in:
Optics Express

Published: 27/11/2017

Document Version:
Final Published version, also known as Publisher's PDF, Publisher's Final version or Version of Record

License:
Unspecified

Published version (DOI):
10.1364/OE.25.029885

Publication details:
PARK, DONGHUN., PAGÁN, VINCENT. R., CHO, PAK. S., LUO, JINGDONG., JEN, ALEX. K-Y., & PETRUZZI, PAUL. V. (2017). RF photonic downconversion of vector modulated signals based on a millimeter-wave coupled electrooptic nonlinear polymer phase-modulator. *Optics Express*, *25*(24), 29885-29895. https://doi.org/10.1364/OE.25.029885

Research Article | Vol. 25, No. 24 | 27 Nov 2017 | OPTICS EXPRESS 29885
Optics EXPRESS

RF photonic downconversion of vector modulated signals based on a millimeter-wave coupled electrooptic nonlinear polymer phase-modulator

DONGHUN PARK,[1,2,*] VINCENT. R. PAGÁN,[1] PAK S. CHO,[1,2] JINGDONG LUO,[3,4] ALEX K.-Y. JEN,[3,4,5] AND PAUL. V. PETRUZZI[1]

[1]*Laboratory for Physical Sciences, College Park, Maryland 20740, USA*
[2]*Deptartment of Electrical and Computer Engineering, University of Maryland, College Park, Maryland 20742, USA*
[3]*Deptartment of Materials Science and Engineering, University of Washington, Seattle, Washington 98195, USA*
[4]*Currently with the Department of Chemistry, City University of Hong Kong, Tat Chee Avenue, Kowloon, Hong Kong, China*
[5]*Currently with the Department of Materials Science and Engineering, City University of Hong Kong, Tat Chee Avenue, Kowloon, Hong Kong, China*
[*]*leomac@lps.umd.edu*

Abstract: We report the RF photonic reception and downconversion of vector modulated RF signals using a millimeter-wave coupled electrooptic phase modulator with in-plane slotted patch antennas based on SEO125 nonlinear polymer. We demonstrate experimental results with QPSK, 8-PSK, 16-QAM, 32-QAM, and 64-QAM millimeter-wave signals centered at 36 GHz. After downconversion to intermediate frequencies between 0.5 GHz and 2 GHz, the vector encoded signals are demodulated using an electrical signal analyzer and found to have measured error vector magnitudes below 8%. Design, simulation, fabrication, and experimental results are presented and discussed.

OCIS codes: (060.5060) Phase modulation; (060.5625) Radio frequency photonics; (130.5460) Polymer waveguides.

References and links

1. H. Shams and A. Seeds, "Optics Photonics, Fiber and THz Wireless Communication," Optics & Photonics News Mar. (2017).
2. J. Capmany and D. Novak, "Microwave photonics combines two worlds," Nat. Photonics **1**, 319–330 (2007).
3. T. R. Clark and R. Waterhouse, "Photonics for RF Front Ends," IEEE Microw. Mag. **12**(3), 87–95 (2011).
4. V. R. Pagán, B. M. Haas, and T. E. Murphy, "Linearized electrooptic microwave downconversion using phase modulation and optical filtering," Opt. Express **19**(2), 883–895 (2011).
5. F. T. Sheehy, W. B. Bridges, and J. H. Shaffner, "60 GHz and 94 GHz Antenna-Coupled LiNbO3 Electrooptic Modulators," IEEE Photonics Technol. Lett. **5**(3), 307–310 (1993).
6. R. B. Waterhouse and D. Novak, "Integrated antenna/electro-optic modulator for RF photonic front-ends," in Microwave Symposium Digest (MTT), 2011 IEEE MTT-S International, pp. 1–4, (2011).
7. Y. N. Wijayanto, H. Murata, and Y. Okamura, "Electrooptic Millimeter-Wave–Lightwave Signal Converters Suspended to Gap-Embedded Patch Antennas on Low-k Dielectric Materials," IEEE J. Sel. Top. Quantum Electron. **19**(6), 3400709 (2013).
8. T. Inoue, T. Ikeda, H. Murata, and Y. Okamura, "Wireless data transfer in 60 GHz-band using array-antenna-electrode electro-optic modulator," IEEE Photonics Conference, pp. 21–22, (2016).
9. H. Aya, T. Inoue, H. Murata, Y. Okamura, Y. N. Wijayanto, A. Kanno, and T. Kawanishi, "Wireless millimeter-wave-lightwave signal converter using stacked patch-antennas embedded with a micrometer-gap and electro-optic crystal," International Conference on Radar, Antenna, Microwave, Electronics, and Telecommunications, pp. 77–80, (2016).
10. O. D. Herrera, K.-J. Kim, R. Voorakaranam, R. Himmelhuber, S. Wang, V. Demir, Q. Zhan, L. Li, R. Norwood, R. Nelson, J. Luo, A. Jen, and N. Peyghambarian, "Silica/Electro-Optic Polymer Optical Modulator with Integrated Antenna for Microwave Receiving," J. Lightwave Technol. **32**(20), 3861–3867 (2014).

#307137 https://doi.org/10.1364/OE.25.029885
Journal © 2017 Received 15 Sep 2017; revised 9 Nov 2017; accepted 9 Nov 2017; published 15 Nov 2017

Optics EXPRESS

11. X. Zhang, A. Hosseini, H. Subbaraman, S. Wang, Q. Zhan, J. Luo, A. K.-Y. Jen, and R. T. Chen, "Integrated Photonic Electromagnetic Field Sensor Based on Broadband Bowtie Antenna Coupled Silicon Organic Hybrid Modulator," J. Lightwave Technol. **32**(20), 3774–3784 (2014).
12. D. H. Park, V. R. Pagán, T. E. Murphy, J. Luo, A. K.-Y. Jen, and W. N. Herman, "Free space millimeter wave-coupled electro-optic high speed nonlinear polymer phase modulator with in-plane slotted patch antennas," Opt. Express **23**(7), 9464–9476 (2015).
13. D. Park, V. Pagán, J. Luo, A. Jen, and P. Petruzzi, "RF Photonic Downconversion of a QPSK Signal with a Millimeter-Wave Coupled Polymer Phase Modulator," in Proceedings of the Conference on Nonlinear Optics, (OSA, 2017), paper NM3A.5.
14. V. R. Pagán, B. M. Haas, and T. E. Murphy, "Linearized electrooptic microwave downconversion using phase modulation and optical filtering," Opt. Express **19**(2), 883–895 (2011).
15. C. A. Balanis, Antenna Theory, 3rd ed. (Wiley-Interscience, 2005).
16. R. Song, H. C. Song, W. H. Steier, and C. H. Cox III, "Analysis and Demonstration of Mach–Zehnder Polymer Modulators Using In-Plane Coplanar Waveguide Structure," IEEE J. Quantum Electron. **43**(8), 633–640 (2007).
17. T. Hirano, K. Okada, J. Hirokawa, and M. Ando, "60 GHz On-Chip Patch Antenna Integrated in a 0.18-μm CMOS Technology," in Proceedings of IEEE International Symposium on Antennas & Propagation (IEEE, 2012), pp. 62–65.
18. J. Luo and A. K.-Y. Jen, "Highly Efficient Organic Electrooptic Materials and Their Hybrid Systems for Advanced Photonic Devices," IEEE J. Sel. Top. Quantum Electron. **19**(6), 3401012 (2013).
19. Optisystem v14.0.2, Optiwave, Inc.
20. R. Shafik, M. Rahman, and A. Islam, "On the Extended Relationships Among EVM, BER and SNR as Performance Metrics," in International Conf. on Electrical and Computer Engineering (2006), pp. 408–411.
21. A. Stöhr, "Photonic millimeter-wave generation and its applications in high data rate wireless access," in Proceedings of the IEEE Topical Meeting on Microwave Photonics (MWP, 2010), pp. 7–10.

1. Introduction

Consumers and service providers demand more bandwidth for a range of image-rich multimedia and mobile applications in the modern network environment [1]. Radio frequency (RF) photonic technologies can potentially meet the demand for wide bandwidth microwave and millimeter-wave (mmWave) distribution, frequency conversion, and detection, among others [2,3]. Radio-over-fiber (RoF) systems offer advantages for optical relay of microwave, mmWave, and terahertz signals over distances where coaxial cable is prohibitively lossy [1–4]. An electrooptic (EO) phase-modulator is promising for reducing the complexity of RF photonic front-ends at millimeter-wave frequencies where the antenna dimensions are small enough for device integration. Various types of wave coupled optical modulators have been reported since Sheehy et al. demonstrated a dipole antenna-integrated $LiNbO_3$ modulator for the first time [5–13]. Recently, a first demonstration of wireless data transfer using a mmWave electrooptic modulator with an integrated antenna array was published [8]. However, reception and photonic downconversion of vector modulated mmWave signals using an antenna-integrated EO modulator (AI-EOM) has not yet been demonstrated up to this point.

We previously reported a mmWave coupled electrooptic phase-modulator operating at a frequency of 36 GHz based on a nonlinear polymer [12, 13] where the carrier-to-sideband ratio (CSR), defined as the difference in power between the optical carrier and the first-order optical sidebands, was 22 dB under an RF excitation of 120 V/m^2. The estimated EO coefficient was 100 pm/V and the figure-of-merit (FOM) was found to be 2.0 $W^{-1/2}$. In this paper, we report a 27 dB improvement in the optical insertion loss of the device by enlarging the antenna slot through careful consideration of the tradeoff between optical loss and enhancement factor. The higher optical power at the device output allows us to downconvert vector modulated mmWave signals centered at 36 GHz to intermediate frequencies (IFs) below 2 GHz. This is key because the optical power into the device cannot simply be increased to compensate for high optical insertion losses without risking device damage. We then show results where phase-shift keyed (PSK) and quadrature amplitude modulation (QAM) signals are electrically demodulated with measured root mean square (RMS) error vector magnitudes (EVM) of 8% or less after being received and downconverted via an RF photonic scheme incorporating our AI-EOM. Furthermore, we analytically model the RF

Optics EXPRESS

photonic downconverting setup and discuss the design, simulation, fabrication, and measurements of our device.

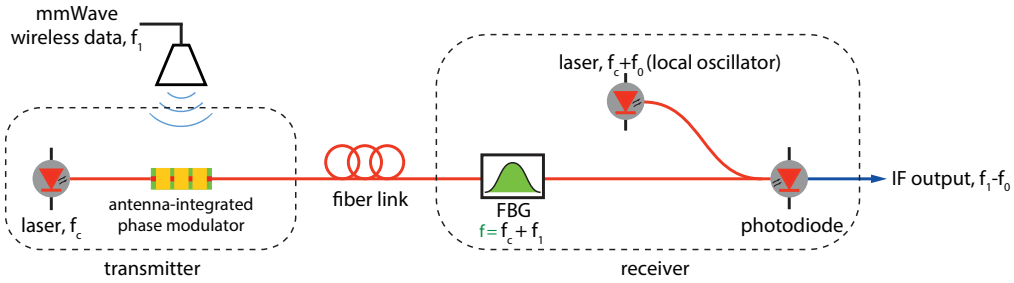

Fig. 1. Schematic of the wireless RoF downconversion link. The antenna-integrated electrooptic modulator optically phase-encodes millimeter-wave signals that are then relayed through a fiber link to a heterodyne optical coherent receiver. In the receiver, a fiber Bragg grating (FBG) in reflection mode (circulator not shown) is used to pass only the first order optical sideband generated via EO phase-modulation. An optical local oscillator is combined with the filtered optical signal to produce beat products at the intermediate frequency (IF) of $|f_1 - f_0|$ with a square-law photodiode.

2. Theory

Figure 1 shows a simplified schematic of the RF photonic scheme used to demonstrate the operation of our AI-EOM. In the transmitter, a continuous-wave (CW) optical wave is electrooptically phase-modulated by a millimeter-wave RF signal as it passes through the AI-EOM. In the receiver, the phase-modulated optical signal is bandpass filtered using a fiber Bragg grating. The reflected signal is routed through a circulator (not shown) and then combined with an optical local oscillator (OLO). The resulting signal is incident on a photodetector to perform heterodyne optical detection.

Ignoring the optical insertion losses of the components and assuming an ideal CW laser for simplicity, the phase-modulated optical signal after the AI-EOM is expressed as [14]

$$u_c(t) = \sqrt{P_c} e^{i\omega_c t} e^{i m_1 \sin \Omega_1 t}, \tag{1}$$

where P_c, ω_c, and Ω_1 are the optical power, the angular frequency of the laser ($\omega_c = 2\pi f_c$), and the angular frequency of the mmWave signal ($\Omega_1 = 2\pi f_1$), respectively. The modulation index is m_1 represented by

$$m_1 = \pi \frac{V_1}{V_\pi}, \tag{2}$$

where V_π and V_1 are the half-wave voltage and the voltage applied to the AI-EOM. Assuming that a linearly polarized antenna having a gain of G is aligned and positioned at a distance r directly above the device, V_1 can be expressed as

$$V_1 = 2t_{RF} E_{inc} \cdot W_{eff} = 2t_{RF} \sqrt{2\eta P_D} \cdot W_{eff} = 2t_{RF} \sqrt{2\eta \frac{P_t \cdot G}{4\pi r^2}} \cdot W_{eff}, \tag{3}$$

where t_{RF}, E_{inc}, η, and P_D are the transverse electric (TE) Fresnel transmission coefficient, the electric field of incident RF signal, the free space impedance, and the electric field power density at the surface of modulator [12]. P_t and W_{eff} are the RF power fed into the antenna and the effective width of the integrated patch antenna in the AI-EOM, respectively. We note that the field in the slotted patch antenna is enhanced by a factor of $2t_{RF}W_{eff}/d_{gap}$, where d_{gap} denotes the slot width. In this manner, the slotted patch antenna without feeding structures

technically acts more like an electric field concentrator than an antenna in the truest sense. More details can be found in [12]. Applying the Jacobi-Anger expansion to Eq. (1) we obtain

$$u_c(t) = \sqrt{P_c}\, e^{i\omega_c t} \sum_n J_n\left(m_1\right) e^{in\Omega_1 t} \tag{4}$$

where the summation runs from negative to positive infinity. At the receiver, the modulated optical signal passes through a fiber Bragg grating (FBG) filter operating in reflection mode having a center angular frequency of $\omega_c + \Omega_1 (= 2\pi f_c + 2\pi f_1)$. The filtered optical signal is combined with a co-polarized optical LO described by

$$u_0(t) = \sqrt{P_{LO}}\, e^{i(\omega_c + \Omega_0)t} \tag{5}$$

and detected with a photodiode having responsivity of R. Assuming the FBG bandpass filter is ideal and passes only the first order sideband of the phase-encoded optical signal, the photocurrent is can be calculated to be

$$i(t) = \frac{R}{2}\left|u_c(t) + u_0(t)\right|^2 = \frac{R}{2}\left[P_c \cdot J_1\left(m_1\right)^2 + P_{LO} + 2\sqrt{P_c P_{LO}}\, J_1\left(m_1\right)\cos\left(\omega_{IF} t\right)\right], \tag{6}$$

where ω_{IF} is the intermediate angular frequency defined as $\left|\Omega_1 - \Omega_0\right| = 2\pi\left|f_1 - f_0\right|$. If the 2x1 polarization maintaining (PM) coupler and photodetector were replaced by a 2x2 PM coupler followed by an ideal balanced detector (not shown in Fig. 1), then the photocurrent can be given by

$$i(t) = R\sqrt{P_c P_{LO}}\, J_1\left(m_1\right)\cos\left(\omega_{IF} t\right) = I_0 \cos\left(\omega_{IF} t\right). \tag{7}$$

The time-averaged downconverted power at the IF through an impedance Z_{out} can then be written as

$$P_{IF} = \frac{1}{2} I_0^2 Z_{out} = \frac{1}{2} Z_{out} R^2 P_c P_{LO} J_1\left(m_1\right)^2. \tag{8}$$

The Bessel function of the first kind of order one can be Taylor expanded as

$$J_1\left(m_1\right) = \sum_{n=0}^{\infty} \frac{(-1)^n}{n!(n+1)!}\left(\frac{m_1}{2}\right)^{2n+1}. \tag{9}$$

Thus, the IF downconverted power is linearly proportional to the input RF power for $m_1 << 1$ because the first term (n = 0) of the series in Eq. (9) is dominant.

Optics EXPRESS

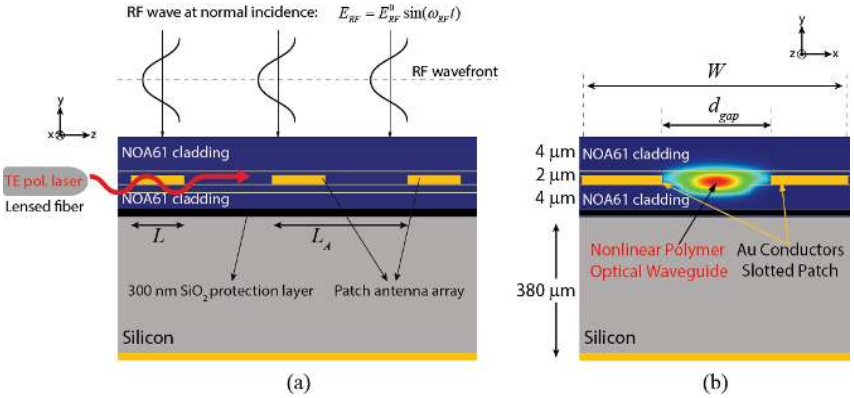

Fig. 2. (Not to scale) (a) Side view (y-z plane) of the antenna-integrated electrooptic modulator with three elements ($N = 3$) and RF plane waves at normal incidence. The antenna length L and the array separation L_A should be carefully designed to accumulate phase-modulation depth as the optical signal propagates through the device. A SiO_2 protection layer on the Si wafer is present to block leakage current through the Si substrate during poling process. (b) Cross section (x-y plane) of the device with the simulated fundamental optical mode profile shown in the center.

3. Design, simulation, and fabrication

Figure 2 shows the schematic of the antenna-integrated EO modulator. An optical ridge waveguide core is positioned between two NOA61 (Norland, Inc.) ultraviolet (UV)-curable polymer cladding layers. The waveguide dimensions are selected to achieve single optical mode operation. Slotted patch antenna elements are deposited on the NOA61 bottom cladding layer. The optical waveguide is routed through the slots in the patch antennas in order to achieve high overlap integral between the optical and RF fields. Since the antennas are also used for poling, this also allows for high poling efficiency. The resonant RF frequency depends on both the width of the patch antenna and the RF index of the substrate. We choose $W = 1.514$ mm for operation near 37 GHz based on Ansoft HFSS® simulations. The closed-form expression $W \approx \lambda_{RF} \Big/ \left[2\sqrt{(\varepsilon_{RF}+1)/2} \right]$ [15], which takes account of the fact that the electromagnetic wave exists above the device, can also be used to estimate the antenna width and provides similar results to the simulation with $\varepsilon_{RF} = 12$. For an RF frequency of 37 GHz and an effective optical index of $n_0 = 1.7$ from mode solver software (OWMS, Apollo Photonics, Inc.), the length of the patch antenna and the array length are given by

$$L = c/(2n_0 f_{RF}) = 2.4 \text{ mm}, \; L_A = 2L = 4.8 \text{ mm}, \tag{10}$$

where c is the speed of light and n_0 the effective optical index. The length of the patch and the spacing of the array structure were designed for normal RF incidence and the angle dependence on antenna array parameters such as length, spacing, and width can be found in [12]. In the design, $L = 2.2$ mm and $L_A = 4.8$ mm were used. The length of patch L is chosen to be slightly smaller than the optimal length of 2.4 mm in order to be consistent with other designs that we have considered. Three array elements ($N = 3$) are used and the length of the patch is 1.3 times longer than the two element device ($N = 2$) reported in [12].

Low loss optical waveguides and antenna structures producing a high field enhancement factor are necessary for efficient electrical-to-optical conversion. The insertion loss and the enhancement factor are both functions of the gap size of the slotted patch antenna. A wider gap decreases the insertion loss and the enhancement factor. Conversely, a smaller gap increases both. Put another way, the enhancement factor affects the carrier-to-sideband ratio while the optical insertion loss preserves the CSR but lowers the power of both the carrier and

Optics EXPRESS

the sidebands. This is similar to the well-known trade-off between V_π in EOMs and optical loss due to metallic electrodes [16]. In the experimental setup, it is important that the first-order sideband power be sufficient to meet the minimum power threshold of the optical amplifier.

We estimate the sideband power as a function of gap size in the patch antenna and length of the optical waveguide in order to find the optimal gap size to produce the highest sideband power. For simplicity of the simulation, we assume an optical input power of 0 dBm, a constant EO coefficient of 100 pm/V, and an overlap factor of 0.7. Figure 3 is a three-dimensional plot showing these results where the metallic waveguide length only represents the waveguide regions between the antennas since the metallic loss contribution dominates the incurred propagation losses. The results indicate that when the antenna array length is 1 cm, which is about the length of our AI-EOM waveguide, the highest sideband power achievable is −37 dBm for a gap size of approximately 17 μm. Furthermore, they show that for a fixed gap size, the sideband power can be increased by making the waveguide longer and adding appropriately spaced antennas for quasi-phase-matching.

Compared with our previous device having a gap size of 10 μm [12], the optical sideband power for a 17 μm gap is estimated to be 27 dB higher. However, it should be noted that as the gap is made larger, a higher poling voltage must be applied in order to achieve the same in-device poling efficiency. The simulation results shown here do not account for limitations in the poling process such as the maximum voltage/current of the DC power supply or damage produced in the device by arcing when the device is poled at high voltages. A lower in-device electrooptic coefficient or higher optical losses due to damage would almost certainly result in reduced optical sideband power. Thus, a 14 μm gap was ultimately chosen as we believe it represents a reasonable trade-off between the optimal design parameters found by simulation and poling considerations in the laboratory. Based on the assumption that the poling efficiency is not a function of the gap size, the penalty in optical sideband power in selecting 14 μm over 17 μm is predicted to be approximately 3 dB.

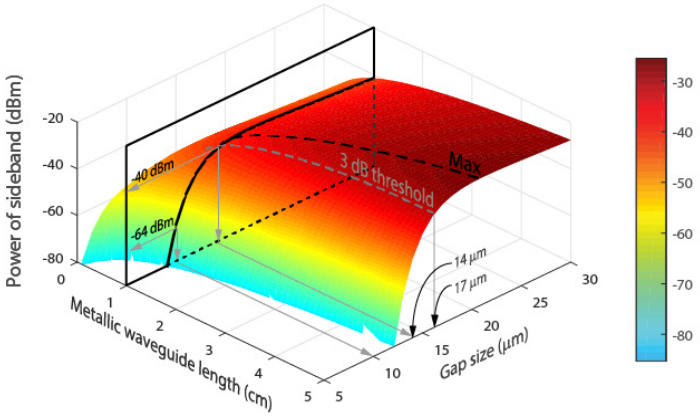

Fig. 3. Simulated optical sideband power as a function of waveguide length and gap size in the antenna-integrated electrooptic modulator. For analytical simplicity, the results assume that the in-device poling efficiency and overlap factor are constant as the device dimensions are scaled. For a 1 cm long metallic waveguide length, the optical sideband powers are −64 dBm and −40 dBm for gap sizes of 10 μm and 14 μm, respectively.

Optics EXPRESS

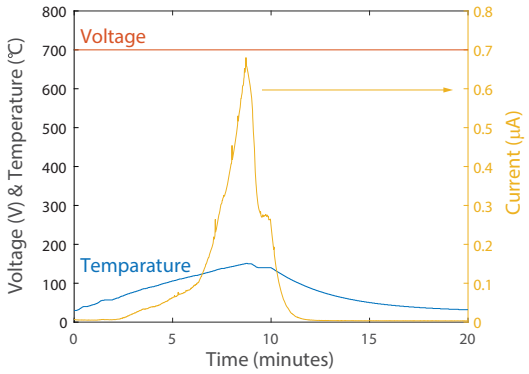

Fig. 4. Poling voltage, current, and temperature with time. The applied voltage is constant during throughout the poling procedure. The temperature is increased slowly up to the glass transition temperature of 150 °C and then the sample is allowed to cool. The maximum current supplied by the poling power supply is 0.66 mA.

A *p*-type Silicon (Si) substrate (<100> single-side polished, University Wafer) with 300 nm SiO_2 by plasma-enhanced chemical vapor deposition (PECVD) is used to minimize leakage current during the poling procedure. A 1-2 μm Au film ground plane for the antenna is electron beam (E-beam) evaporated on the back side of the Si substrate, as opposed to being placed immediately under the lower optical waveguide cladding layer, in order to increase the bandwidth and antenna efficiency due to the thicker antenna substrate [17]. A 4 μm thick NOA61 UV curable polymer is spin-cast onto the Si substrate and cured under UV light having an intensity of 11-13 mW/cm^2 for 5 minutes. Ridge waveguides are patterned on the photo-resist. The patterns are then processed by reactive ion etch (RIE) to obtain 1 μm deep and 4 μm wide trenches using O_2 gas. The 1.2 μm thick Ti/Au for the slotted patch antenna structure is deposited on the bottom cladding layer using an E-beam evaporator. A nonlinear polymer thin film, SEO125 [18], is formulated by doping 35 wt. % of AJLZ53 to COPS host polymer dissolved in dibromomethane. The solution is filtered with a 0.2 μm polytetrafluoroethylene (PTFE) membrane filter.

The nonlinear polymer solution is spin-coated on the patterned bottom cladding with metallic antennas to achieve a height of 1.8-2 μm in the waveguide core, which supports only a single optical mode. Residual solvent is evaporated after post-baking at 120 °C for 5 minutes. The device is further baked at 80 °C inside a vacuum oven for over 24 hours and finally another 4 μm top cladding of NOA61 is spin-cast and UV-cured. The slotted patch antenna structure is used as a poling electrode to orient the chromophore molecules in the nonlinear polymer waveguide near the glass transition temperature of 150 °C under nitrogen environment. The maximum DC applied voltage is ~700 V (50 V/μm) and the peak poling current was 0.68 μA, as shown in Fig. 4. Finally, the device is diced to produce optical input and output facets and cleaved/diced to remove Ti/Au poling leads. While we did not observe any significant degradation in the devices during our measurements, we also did not study this since the temporal stability of poled SEO125 has already been reported in [18].

4. Results

The RF photonic experimental setup to receive, downconvert, and electrically demodulate a vector encoded mmWave signal at 36 GHz using an antenna-integrated electrooptic modulator is shown in Fig. 5. A function generator (MXG vector signal generator, Agilent) produces a 1 MBaud quadrature-phase shift keyed (QPSK) signal with a 2 GHz carrier. The QPSK signal is then upconverted from 2 GHz to 36 GHz by mixing it with a 34 GHz electrical local oscillator (LO). The resulting signal is filtered with an 18 GHz high pass filter (FH1800, Marki Microwave) and amplified using a broadband low noise amplifier (SHF810,

Optics EXPRESS

SHF Communication Technologies AG) followed by a 30-40 GHz RF power amplifier (AP3040-33, Microwave Dynamics). The signal is then sent into a 20 dBi standard gain rectangular horn antenna (SH128-20, Fairview Microwave). The horn is positioned approximately 23 cm directly above the AI-EOM and aligned such that the radiated electric field component is perpendicular to the antenna slots.

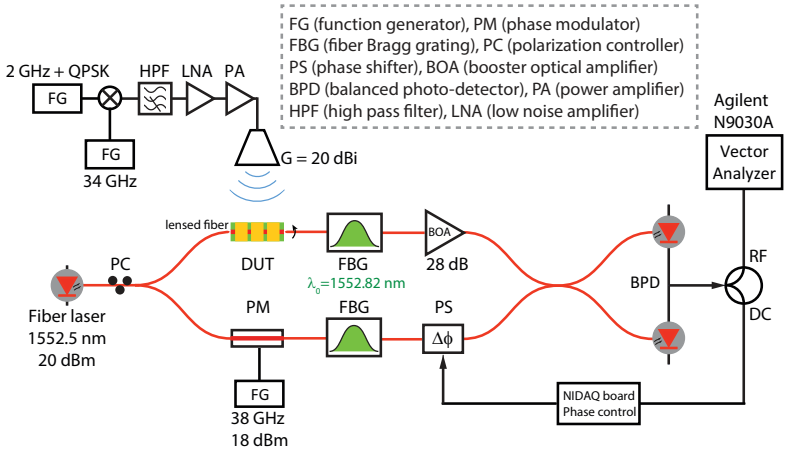

Fig. 5. Schematic showing the RF photonic downconversion experimental setup. Mach-Zehnder interferometric method is used to demonstrate RoF communication via vector modulation.

To measure the optical carrier-to-sideband ratio, a pure RF tone at 36 GHz is electrically generated by turning off the QPSK modulation on the 2 GHz function generator. The equivalent isotropic radiated power (EIRP) from the horn antenna is estimated to be 40 dBm resulting in a power density of 15 W/m^2 at the top surface of the AI-EOM. Using an optical spectrum analyzer (OSA), the CSR is determined to be approximately 38 dB as indicated in Fig. 6. This translates to a modulation index of approximately m = 0.03 radians. After normalizing for differences in the power densities between our experimental setups, our new device has an overall measured electrooptic conversion efficiency that is approximately 6 dB lower than our previous device. We believe that this is primarily due to a lower in-device poling efficiency of the wider gap device. The resulting figure of merit for our new antenna-integrated electrooptic phase modulator is estimated to be

$$\mathrm{FOM}[\mathrm{W}^{-1/2}] = \frac{m}{\pi}\left(P_D \frac{\lambda_{RF}^2}{4\pi}\right)^{-\frac{1}{2}} = 1.1\,\mathrm{W}^{-1/2}. \tag{11}$$

Note we have made a correction to the FOM equation published in [12].

Optics EXPRESS

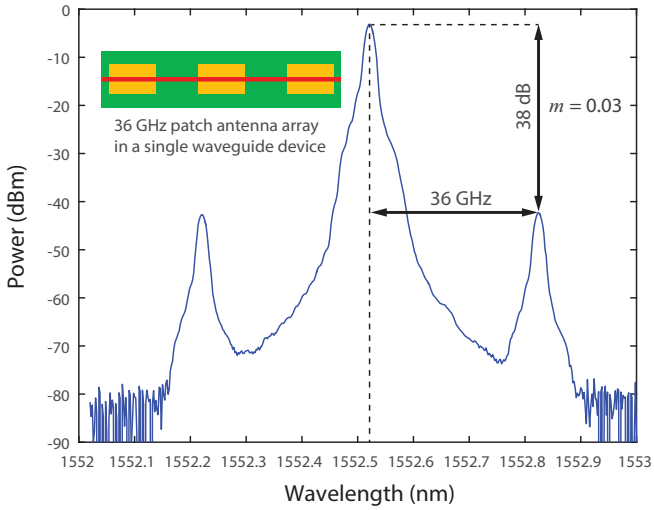

Fig. 6. Optical spectrum of a three element (N = 3) antenna-integrated electrooptic modulator under RF illumination. The horn antenna is positioned 23 cm above the device and the effective isotropic radiated power (EIRP) is approximately 40 dBm. The resulting CSR is 38 dB, corresponding to modulation index m = 0.03 rad [12].

A commercial fiber laser (Rock Module, NP photonics, Inc.) centered at 1552.5 nm having a linewidth below 1 kHz is divided with a 1 × 2 polarization maintaining (PM) splitter into two paths. The optical signal in the upper arm is sent to the AI-EOM and the optical signal in the lower arm is sent into a commercial phase modulator. An RF tone with a frequency of 38 GHz is applied to a commercial electrooptic phase modulator. PM fiber Bragg gratings (C91547, TeraXion) in reflection mode are used in both arms as optical bandpass filters nominally centered at 1552.82 nm to select the upper first order optical sidebands generated via EO phase modulation. The optical signal emerging from the FBG in the upper arm is amplified with a PM booster optical amplifier (S9FC1080P, Thorlab, Inc.). The signals in the two arms are then combined with a 2 × 2 PM coupler and sent into a balanced photodetector (1617-AC-FC, Newport, Inc.). The resulting photocurrent contains a direct current (DC) component and a signal centered at the IF of 2 GHz. To minimize received signal fading caused by environmental (i.e. thermal and vibrational) effects, the optical fiber path was partially stabilized using a PM optical phase shifter (PS) in the lower arm driven by a feedback circuit.

The incident RF power on the device is swept by controlling the RF power of the 2 GHz function generator. The measured and simulated downconverted powers at the intermediate frequency of 2 GHz as functions of the RF transmit power are shown in Fig. 7(left). The simulated results using OptiSystem [19] seem to be in good agreement with the experimental results. The RF-to-IF transfer function is linear for small incident RF signal amplitudes since $J_1(m) \approx m/2$ for $m << 1$ in Eq. (8). However, as predicted by theory, it becomes nonlinear for large input amplitudes. Figure 7(right) shows the received QPSK constellation and the downconverted electrical spectrum for a RF transmit power of 18 dBm at the horn antenna and an electrical LO power of 15 dBm. The error vector magnitude of the downconverted signal is found to be less than 8% using a vector signal analyzer. Assuming Gaussian noise, the BER can be estimated to be less than 10^{-6} indicating that the data could potentially be recovered error-free [20].

Optics EXPRESS

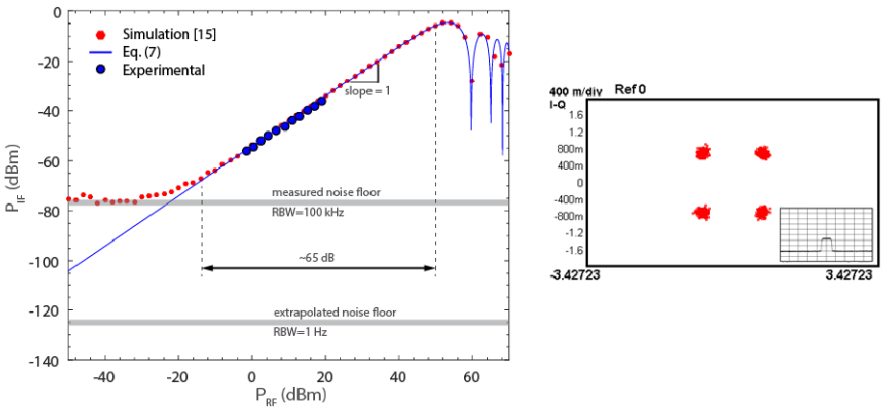

Fig. 7. (left) Measured (blue) and simulated (red) downconverted powers as a function of the incident RF power for the antenna transmitter. The blue line is calculated based on Eq. (7). (right) Measured constellation diagram of 1 MBaud QPSK signal at an intermediate frequency of 2 GHz having a measured EVM of 8%. The IF spectrum is shown in the inset (10 dB/div and 10 MHz span).

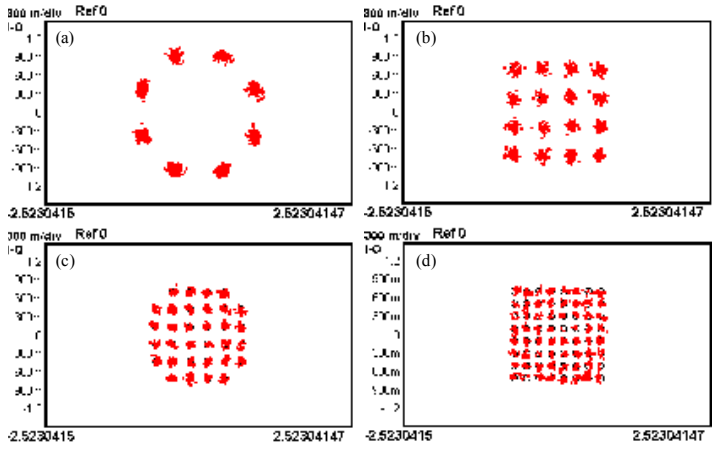

Fig. 8. Constellation diagrams for additional modulation formats measured using the RF downconversion setup with an antenna-integrated, electrooptic modulator (a) 8-PSK (7.8%), (b) 16-QAM (7.3%), (c) 32-QAM (5.1%), and (d) 64-QAM (4.8%) at the intermediate frequency of 0.5 GHz. All signals have a symbol rate of 1 MBaud and estimated BERs below 10^{-5}.

The RF photonic downconversion setup using the AI-EOM is also found to support higher order phase-shift keyed and quadrature amplitude modulation signals. The measured constellations for 8-PSK, 16-QAM, 32-QAM, and 64-QAM signals all having a symbol rate of 1 MBaud are shown in Fig. 8. Higher order modulations allow more data to be transmitted in a given bandwidth; however, they also require higher SNRs for a given BER. The measured EVMs for all of the signals were less than 8% and estimated BERs are all below 10^{-5}. Based on the components used, we believe that the 3 dB electrical bandwidth of our AI-EOM should set the limit on the maximum symbol rate that can be received and downconverted.

To indirectly deduce the bandwidth of our AI-EOM, the EVMs and the IF powers are measured as the mmW RF carrier frequency is swept. In this experiment, a 1 MBaud QPSK signal is used and the measured results are shown in Fig. 9. As can be clearly observed, the IF power reached a maximum at 36 GHz, which corresponded to the resonant frequency of the patch antenna. The EVM is also minimum at this frequency and agrees with the expected

Optics EXPRESS

behavior as the RMS EVM is approximately inversely proportional to the square-root of the SNR [20]. From this measurement, a total RF bandwidth of 2 GHz is estimated agreeing with our prior reported estimates in [12] based on CSR measurements. Although this experiment does not definitively prove that our device is capable of supporting gigabit date rates; it does suggest that it may have the potential to do so.

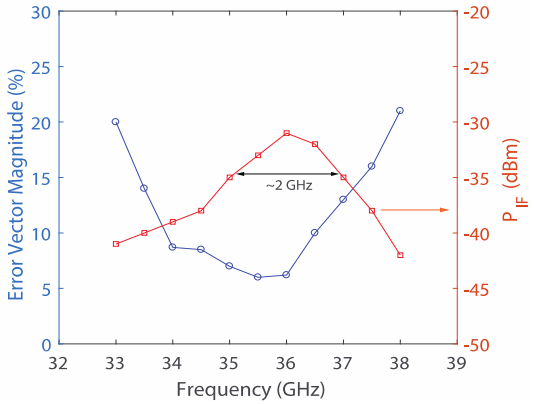

Fig. 9. Measured RMS error vector magnitudes (blue) and downconverted RF powers (red) at the intermediate frequency of 0.5 GHz as a function of a QPSK encoded mmWave signal center frequency. The symbol rate is 1 MBaud.

5. Conclusions

We have discussed the design and fabrication of a mmWave-coupled slotted patch antenna-integrated electrooptic phase-modulator based on nonlinear polymer SEO125. We estimate that the device has an EO coefficient of 50 pm/V and a total insertion optical loss of less than 13 dB. A modulation index of 0.03 rad was calculated based on measuring the optical carrier-to-sideband ratio with an RF power density of 15 W/m^2 at the top surface of the device leading to a device figure-of-merit of 1.1 $W^{-1/2}$. Wider gaps in the slotted antennas result in lower optical insertion losses. However, this also leads to a reduction in the enhancement factor and lowers the in-device poling efficiency resulting in higher carrier-to-sideband ratios (CSRs). We selected the gap size based on these considerations and were able to fabricate a device that we could subsequently use to perform RF photonic downconversion of 1 MBaud vector encoded millimeter-wave signals. To our knowledge, this is the first time that an antenna-integrated polymer electrooptic phase-modulator has been incorporated in any RF photonic experimental setup and used to demonstrate reception of mmWave signals and the first time that such a device made using any material system has been used for RF photonic reception and downconvertion of vector-encoded mmWave signals. Furthermore, we have shown that our device works with higher-order modulation formats such as 8-PSK, 16-QAM, 32-QAM, and 64-QAM in addition to QPSK. Based on these encouraging results, future measurements using higher-speed test equipment are currently being considered. We believe that this device may be promising for future mmWave wireless networks such as those described in [21].

Acknowledgments

We thank Victor Yun, Yongzhang Leng, Chi Lee, William Astar, and Julius Goldhar for help with the experimental setup, the fabrication, the data analysis, and the suggestions.